Crystallization of manganese (V) oxides by hydroflux synthesis: Control of anisotropic growth and electrochemical stability

Carlos V. M. Inocêncio,[a] Almudena Torres-Pardo,[b] David Montero,[c] Lucien Roach,[d] Pierre-Olivier Autran,[e] Capucine Sassoye,[a] Cyril Aymonier,[d] Aurea Varela [b], Marina Parras,[b] Christel Laberty-Robert[a] and David Portehault[a,*]

[a] *Sorbonne Université, CNRS, Laboratoire de Chimie de la Matière Condensée de Paris (LCMCP), 4 place Jussieu, F-75005 Paris, France*

[b] *Departamento de Química Inorgánica, Facultad de Ciencias Químicas, Universidad Complutense, 28040 Madrid, Spain*

[c] *Fédération de chimie et matériaux de Paris-centre (FCMat), Sorbonne Université, 4 Place Jussieu, F-75005 Paris, France*

[d] *Université Bordeaux, CNRS, Bordeaux INP, ICMCB, UMR 5026, Pessac, 33600, France*

[e] *European Synchrotron Radiation Facility (ESRF), 38043 Grenoble, France*

*Corresponding author: david.portehault@sorbonne-universite.fr

https://doi.org/10.26434/chemrxiv-2024-lk8q5 **ORCID:** https://orcid.org/0000-0003-4914-4913 Content not peer-reviewed by ChemRxiv. **License:** CC BY 4.0

Abstract

Despite intriguing optical, magnetic, and redox properties, inorganic materials containing pentavalent manganese (Mn^{5+}) are rare and could never be designed as shape-controlled crystals, which limits the ability to tune properties. Herein, we explore alkali hydroxide mixtures with controlled water content, namely hydrofluxes, to demonstrate phase, shape, and nanostructure control of Mn(V) oxides. We demonstrate speciation among $KSrMn^{V}O_4$, $Sr_5(Mn^{V}O_4)_3OH$, and $SrMn^{IV}O_3$ with the water content, the strontium content, and the nature of the alkali cation of the hydroxide salt. We then provide evidence of the key role of water in enabling shape and nanostructure control, which we relate to the preferential interaction of water with specific crystal facets of the hydroxyapatite $Sr_5(Mn^{V}O_4)_3OH$, and to the impact of water on precursor solubility in water-poor hydrofluxes. We then show that nanostructured Mn(V) hydroxyapatite possesses an acid-base redox stability window enabling electrochemical operation in strongly oxidative conditions. By correlating fundamental knowledge of hydrofluxes with crystallization mechanisms, this work sheds light on the possibilities offered by hydrofluxes for crystal shape, size and property control.

https://doi.org/10.26434/chemrxiv-2024-lk8q5 **ORCID:** https://orcid.org/0000-0003-4914-4913 Content not peer-reviewed by ChemRxiv. **License:** CC BY 4.0

Introduction

Manganese can be found in various oxidation states in solid-state materials, from 0 to +7.[1] Despite its low stability and scarcity, pentavalent manganese (V) is at the origin of important properties. It can be used to design colorful blue or green pigments.[2,3] Mn(V) compounds have been considered as laser materials,[4] and also raise interest due to intriguing magnetic properties.[5,6] Mn(V) is also involved in the oxygen-evolving complex for the production of dioxygen during photosynthesis.[7,8] This suggests that Mn(V) compounds could find interest for use in water oxidation electrocatalysis, provided that they can be used in conditions where the oxidation state and structural features are maintained. To date, the electrochemical properties, especially the pH-potential stability window of Mn(V) compounds have not been evaluated, so the feasibility of using Mn(V) compounds for electrochemical applications remains an open question.

Inorganic compounds containing pentavalent manganese (Mn^{5+}) are scarce due to their low stability.[9] Currently reported manganese oxides built on Mn(V) are $Ba_3Mn_2O_8$,[5,6] $KBaMnO_4$,[9] $Ba_5(MnO_4)_3OH$,[10] $Ba_5(MnO_4)_3X$ (X = Cl,[11,12] F[12,13]), $KSrMnO_4$,[14] $Sr_5[MnO_4]_3OH$,[9,10] and its derivatives $Sr_5[(Mn_{1-x}Si_x)O_4]_3(OH)_{1-3x}$ ($x = 0.053$),[9] $Sr_5(MnO_4)_3(OH)_{1-y}F_y$ ($y = 0.90$),[9] and $Sr_5[(Mn_{1-x}Si_x)O_4]_3F_{1-3x}$ ($x = 0.058$).[9] In all these compounds, Mn(V) is found in tetrahedral coordination, $Mn^VO_4^{3-}$, and always in combination with alkali (A) and/or alkaline-earth (AE) metal ions, barium and strontium, as these elements exhibit a basicity high enough to stabilize Mn^V-O bonds with a strong covalent character.[9] In this work, we focus on the Sr-Mn-O system, that encompasses two structural entries: $KSrMnO_4$ and $Sr_5(MnO_4)_3OH$ (**Figure 1**). $KSrMnO_4$ has an orthorhombic structure built on [SrO_8] polyhedra[14] sharing corners and edges with Mn tetrahedra. $Sr_5(MnO_4)_3OH$ exhibits the hexagonal structure typical of hydroxyapatites, with [SrO_9] polyhedra linked to $[MnO_4]^{3-}$ tetrahedra to form channels in the c direction with additional Sr^{2+} cations inside and hydroxyl species in the center.

Synthesis pathways to Mn(V) compounds have traditionally relied on solid-state reactions at temperatures about 1000 °C,[12,13,15] but for the last decade, syntheses down to 250 °C have been made possible by using aqueous precipitation in highly alkaline solutions,[9] and by developing hydroflux approaches.[10,14] In its common occurrence, a hydroflux is a mixture of alkali hydroxide with small amounts of water that enables a dramatic decrease of the melting point compared to the pure hydroxide melt.[10,14] The hygroscopic salt retains water even at elevated temperatures, so that the water vapor pressure is also well below that achieved in hydrothermal conditions. Therefore,

https://doi.org/10.26434/chemrxiv-2024-lk8q5 ORCID: https://orcid.org/0000-0003-4914-4913 Content not peer-reviewed by ChemRxiv. License: CC BY 4.0

a hydroflux retains some of the properties of the parent molten hydroxide, like its high basicity and ability to dissolve a wide range of oxides, but the use of controlled amounts of water provides additional versatility, especially the possibility to tune the acid-base properties of the medium, hence possibly the concentration of reactive species, their speciation and product selection. Consequently, the use of hydroflux synthesis has resulted in the discovery of $KBaMn^{V}O_4$[10] and $KSrMn^{V}O_4$,[14] which could not be achieved by any other approach.

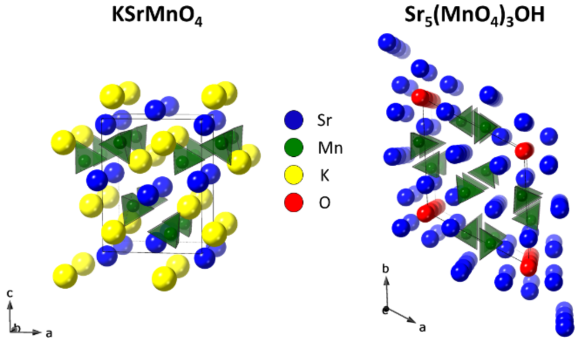

Figure 1. Crystallographic structures of $KSrMnO_4$ and $Sr_5(MnO_4)_3OH$. The green tetrahedra correspond to $[Mn^{V}O_4]^{3-}$ which contains one manganese atom at the center and one oxygen at each vertex. Red spheres represent the O4 oxygen atoms from hydroxyl groups located in the hydroxyapatite channels. For the sake of clarity, oxygen atoms forming the $[MnO_4]^{3-}$ tetrahedra are not displayed. Blue and yellow spheres correspond to strontium and potassium atoms, respectively.

While the ability to select the nature of the Mn(V) oxide has been demonstrated by tuning the composition of hydrofluxes and of the reaction mixtures,[10,14] the exact role of water has not been deciphered. More importantly, the possibility of using hydrofluxes to control crystal size and shape has never been questioned.

Herein, we explore hydroflux synthesis of manganese (V) compounds, by screening experimental parameters. We especially question the influence of water and hydroxide contents on phase speciation. We demonstrate the ability to control crystal shape anisotropy for the Mn(V) hydroxyapatite and to change crystallization pathways to isolate nanostructured hydroxyapatite. We then evaluate the electrochemical stability of this typical manganese (V) material.

Results and discussion

https://doi.org/10.26434/chemrxiv-2024-lk8q5 ORCID: https://orcid.org/0000-0003-4914-4913 Content not peer-reviewed by ChemRxiv. License: CC BY 4.0

Mapping of phase speciation in Sr-Mn-O system

The synthesis procedure relies on the reduction of the permanganate ion ($\mathrm{Mn^{VII}O_4^-}$) towards $\mathrm{Mn^{V}O_4^{3-}}$ in the strongly alkaline environment of a hydroflux made of potassium or sodium hydroxides, water, and strontium salts,[14] as described in equation **(1)**. These conditions are necessary to stabilize Mn(V).[16]

$$2\,[\mathrm{Mn^{VII}O_4}]^- + 4\,\mathrm{OH^-} \rightarrow 2\,[\mathrm{Mn^{V}O_4}]^{3-} + \mathrm{O_2} + 2\,\mathrm{H_2O} \qquad \textbf{(1)}$$

The reaction is performed at 230 °C in an autoclave. To map phase speciation in hydrofluxes (**Figure 2A-B**), we screened the $\mathrm{H_2O}$:(A)OH (A = K, Na) and Sr:Mn elemental ratios, hereafter noted $q(\mathrm{H_2O})_A$ and $q(\mathrm{Sr})$. Contrary to previous reports,[14] we maintained the (A)OH:Mn ratio (equal to *ca.* 211) across all reaction conditions. The nature of the crystalline products was identified by powder X-ray diffraction (XRD) patterns (**Figures S1** to **S3** and **Table S1** in **supplementary information**). The corresponding speciation of major products is depicted in **Figure 2** for KOH- (**Figure 2A**) and NaOH-based (**Figure 2B**) hydrofluxes. According to XRD (**Figure 2C**), $\mathrm{Sr_5(MnO_4)_3OH}$ is obtained at ($q(\mathrm{H_2O})_\mathrm{K}$, $q(\mathrm{Sr})$) = (2.8,4.0) and ($q(\mathrm{H_2O})_\mathrm{Na}$, $q(\mathrm{Sr})$) = (2.8,4.0), $\mathrm{KSrMnO_4}$ and $\mathrm{SrMnO_3}$ are obtained at ($q(\mathrm{H_2O})_\mathrm{K}$, $q(\mathrm{Sr})$) = (1.6,1.0) and ($q(\mathrm{H_2O})_\mathrm{Na}$, $q(\mathrm{Sr})$) = (1.6,1.0), respectively. These results expand those previously reported by Albrecht *et al.*[14] only for KOH hydrofluxes and for $q(\mathrm{Sr}) \leq 1$.

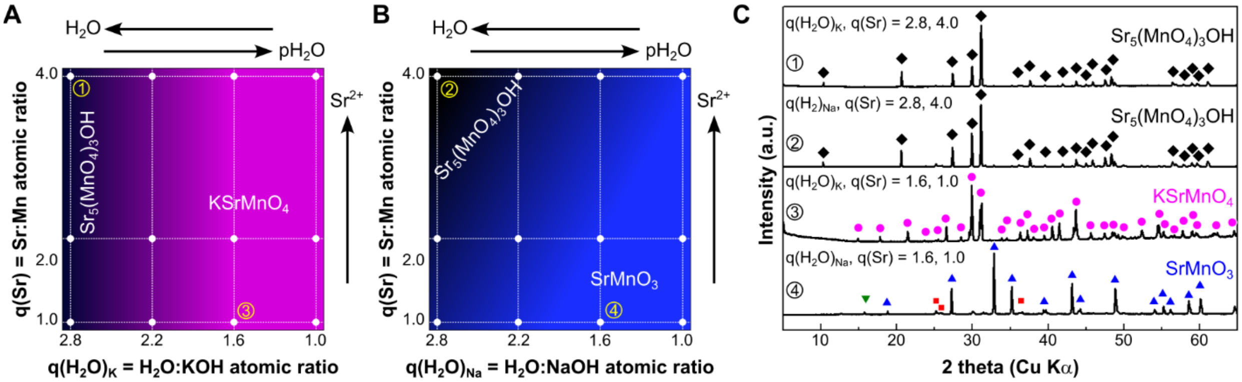

Figure 2. Major phase speciation in KOH and NaOH hydroflux systems. Speciation diagrams for (A) KOH- and (B) NaOH-based hydrofluxes are drawn according to powder XRD. Characteristic XRD patterns for the products are displayed in (C) for positions 1, 2, 3, and 4 spotted in the speciation diagrams. The whole XRD data used to plot figures (A) and (B) are shown in **Figures S1** to **S3**. Each intersection of vertical and horizontal dashed lines indicates an experimental point. In C, the red squares and green triangle correspond to $\mathrm{SrCO_3}$ impurities and $\mathrm{Na_{0.7}MnO_2}$ impurities, respectively.

https://doi.org/10.26434/chemrxiv-2024-lk8q5 **ORCID:** https://orcid.org/0000-0003-4914-4913 Content not peer-reviewed by ChemRxiv. **License:** CC BY 4.0

The KOH hydroflux favors phases containing pentavalent manganese oxide for all compositions studied. $q(\mathrm{Sr})$ shows no influence on the major phase. On the contrary, $q(\mathrm{H_2O})_\mathrm{K}$ clearly affects the nature of the product, from the hydroxyapatite $Sr_5(MnO_4)_3OH$ when $q(\mathrm{H_2O})_\mathrm{K} \geq 2.2$ to $KSrMnO_4$ for $q(\mathrm{H_2O})_\mathrm{K} \leq 1.6$ (**Figures 2A**, **S1-S3** and **S4**). Note that the K:Mn ratio is identical in all experiments, with a large excess of potassium (K:Mn = 211 at. ratio), so the speciation is directly linked to the water content.

Indeed, hydroxide-based hydrofluxes undergo auto-dissociation of hydroxyl ions according to equation **(2)**,[17] which underlies the concept of Lux-Flood oxo-acidity of melts:[18]

$$2\ \mathrm{OH^-} \rightleftarrows \mathrm{O^{2-}} + \mathrm{H_2O} \qquad (\mathbf{2})$$

The oxide ion then appears as a base and water plays the role of acidic species. The auto-dissociation product K_d defines the acidity of the hydroxide melt, according to equations **(3)** to **(5)**:[19]

$$K_\mathrm{d} = [\mathrm{H_2O}] \times [\mathrm{O^{2-}}] \qquad (\mathbf{3})$$

$$\mathrm{pH_2O} = -\log_{10}[\mathrm{H_2O}] \qquad (\mathbf{4})$$

$$\mathrm{p}K_\mathrm{d} = \mathrm{pH_2O} + \mathrm{pO^{2-}} \qquad (\mathbf{5})$$

Therefore, the oxo-acidity of the hydroflux can be adjusted by the water content: the higher the water content (lower $\mathrm{pH_2O}$), the more acidic the medium. An acidic hydroflux has a $\mathrm{pH_2O}$ value below half of the $\mathrm{p}K_\mathrm{d}$ value, on the contrary, if $\mathrm{pH_2O}$ is higher it is basic. If $\mathrm{pH_2O} = \mathrm{p}K_\mathrm{d}/2$, the hydroflux is neutral. K_d depends on the temperature and the alkali cation. For example, K_d is 5 orders of magnitude higher for NaOH-based hydrofluxes than for KOH-based ones at 230 ºC.[17]

Because the K:Mn ratio is maintained in all syntheses described in **Figure 2**, the speciation in KOH-based hydrofluxes is related to the oxo-acidity of the medium: increased acidity (decreased $\mathrm{pH_2O}$ and increased $q(\mathrm{H_2O})_\mathrm{K}$) favors $Sr_5(MnO_4)_3OH$ over $KSrMnO_4$. No data are available on the solubility and speciation of Sr^{2+} in hydrofluxes nor in molten hydroxides, but Zur Loye *et al*. discussed the solubility of other metals in hydrofluxes as a function of $\mathrm{pH_2O}$,[17] where acidic conditions favor the solubilization of metal cations. One can then hypothesize that as acidity decreases ($\mathrm{pH_2O}$ increase), the concentration of Sr^{2+} concentration decreases, which triggers a switch of phase speciation from a Sr-rich Mn(V) phase ($Sr_5(MnO_4)_3OH$) to a Sr-poor one ($KSrMnO_4$). The liquid-phase speciation may also change, the mixture becoming more efficient as an alkali donor as $\mathrm{p}(\mathrm{H_2O})_\mathrm{K}$ increases.[14,17] We also note that increasing the oxo-basicity ($\mathrm{pH_2O}$

https://doi.org/10.26434/chemrxiv-2024-lk8q5 ORCID: https://orcid.org/0000-0003-4914-4913 Content not peer-reviewed by ChemRxiv. License: CC BY 4.0

increase and $q(H_2O)_K$ decrease) promotes the precipitation of $SrCO_3$ carbonate byproducts (**Figures S1-S5**), in a similar manner to aqueous solutions and Brönstedt basicity, which parallels the hypothesis of decreased Sr^{2+} solubility as pH_2O increases.

Contrary to $q(H_2O)_K$, $q(Sr)$ has no influence in the major phase speciation in the KOH-based hydrofluxes but still impacts the nature of the impurities (**Table S1** and **Figure S6**). Firstly, an increase in the relative XRD peak intensities of $SrCO_3$ is observed with the increase of $q(Sr)$ for $q(H_2O)_K \leq 2.2$, which is reasonable due to the increasing amount of strontium introduced. Secondly, significant amounts of $SrMnO_3$ are observed at $q(Sr) = 1$ for $q(H_2O)_K \geq 2.2$. It is likely resulting from the deficiency of strontium in comparison to the $Sr_5(MnO_4)_3OH$ stoichiometry, while the Sr:Mn ratio matches exactly the $SrMnO_3$ stoichiometry.

In NaOH-based hydrofluxes, the final product is affected by both $q(H_2O)_{Na}$ and $q(Sr)$ (**Figures 2B**, **S1-S3** and **S5**). A Mn(V)-containing phase, $Sr_5(MnO_4)_3OH$, can only be obtained at high $q(H_2O)_{Na}$ and/or high $q(Sr)$. As in KOH-based hydrofluxes (**Figure 2A**), the Mn(V) hydroxyapatite is favored at increasing acidity ($q(H_2O)_{Na}$). As a general trend, a q(Sr) increase favors $Sr_5(MnO_4)_3OH$ at the expense of $SrMnO_3$ (**Figure 2B-C**, details in **Figure S7**). Besides, $Na_{0.7}MnO_2$ appears for low Sr contents ($q(Sr) = 1$). No Na-containing phase analogous to $KSrMnO_4$ is reported, so that in the low $q(H_2O)_{Na}$ region (≤ 1.6), if the Sr content is low ($q(Sr) \leq 2$), no Mn(V) phase can forms and the perovskite $SrMn^{IV}O_3$ is obtained. If $q(Sr)$ increases ($q(Sr) = 4$), the large excess of strontium enables stabilization of the hydroxyapatite $Sr_5(MnO_4)_3OH$.

More surprising is the speciation at high water contents ($q(H_2O)_{Na} \geq 2.2$). Indeed, for $q(Sr)$ values above the Sr:Mn stoichiometry in the hydroxyapatite composition, i.e. $q(Sr) \geq 2$, $Sr_5(MnO_4)_3OH$ is the major product in both KOH- and NaOH-based hydrofluxes, as expected. On the contrary, for compositions with $q(Sr) = 1$, the dominant phase is $Sr_5(MnO_4)_3OH$ and $SrMn^{IV}O_3$ in K- and Na-containing hydrofluxes, respectively. This demonstrates the importance of the alkali metal hydroxide choice, even if the product does not contain any alkali metal in its nominal composition.

In the presence of dissolved oxygen, reactions **(6)** and **(7)** occur in molten hydroxides,[17] forming peroxides and superoxides anions:

$$O_{2\,(sol)} + 4\,OH^-_{(l)} \rightleftarrows 2\,O_2^{2-}{}_{(sol)} + 2\,H_2O_{(sol)} \qquad \textbf{(6)}$$

$$3\,O_{2\,(sol)} + 4\,OH^-_{(l)} \rightleftarrows 4\,O_2^-{}_{(sol)} + 2\,H_2O_{(sol)} \qquad \textbf{(7)}$$

https://doi.org/10.26434/chemrxiv-2024-lk8q5 ORCID: https://orcid.org/0000-0003-4914-4913 Content not peer-reviewed by ChemRxiv. License: CC BY 4.0

One can expect that both reactions occur as well in the hydroflux environments studied herein. In the process we developed, oxygen molecules from air are trapped in the reactor when the autoclave is sealed. In the specific case of the syntheses performed here, oxygen arises also from reaction **(1)**. The stabilization of these dissolved strong oxidizing agents varies with the alkali metal:[17] sodium hydroxide stabilizes the peroxide species (reaction **(2)**), while potassium hydroxide stabilizes both peroxide and superoxide (reactions **(2)** and **(3)**). For this reason, the KOH-based hydroflux promotes a more oxidizing environment than the NaOH-based hydroflux and favors a Mn(V) phase, contrary to the NaOH system. This explains the phase speciation between $Sr_5(Mn^{V}O_4)_3OH$ and $SrMn^{IV}O_3$ in the $q(H_2O)_A \geq 2.2$ and $q(Sr) = 1$ region. Furthermore, increased oxidation power is consistent with the fact that pentavalent manganese is present in all major phases obtained from KOH-based hydrofluxes, contrary to the NaOH-based ones, where the main products involve tetravalent manganese for some initial compositions (**Figure 2A-B**).

Anisotropy in the $Sr_5(MnO_4)_3OH$-based hydroxyapatite

The hydroxyapatite obtained from most reaction mixtures displayed in **Figures 2A-B** show XRD patterns (**Figures S1-S3**) corresponding to the $Sr_5(MnO_4)_3OH$ structure but with significant discrepancies in relative intensities compared to those expected from the tabulated structure. These patterns were recorded with a flat XRD holder geometry and exhibit especially an inversion of relative intensities between the {211} ($2\theta_{Cu} = 29.9°$ / $Q = 2.1$ Å^{-1}) and the {300} diffraction peaks ($2\theta_{Cu} = 31.1°$ / $Q = 2.2$ Å^{-1}) versus the simulated pattern, as evidenced with the ($q(H_2O)_K$, $q(Sr)$) = (2.8, 4.0) conditions (**Figure 3A,** flat geometry). All {*kl*0} reflections are indeed overexpressed compared to the simulated pattern, suggesting their preferential exposure. When using a sample holder geometry minimizing preferential orientation (**Figure 3A**, capillary geometry in transmission mode under synchrotron radiation), the relative intensities expected from the tabulated structure are recovered. These results are consistent with anisotropic growth along the ***c*** axis that corresponds to the direction of hydroxyapatite channels. Accordingly, SEM (**Figure 3B**) shows hexagonal microrods. The hexagonal cross-section is fully consistent with the hexagonal crystal structure and its 6-fold axis along ***c***, yielding exposure of {100} lateral facets. Note that anisotropic growth of $Sr_5(MnO_4)_3OH$ microrods could not be achieved previously, whether by aqueous precipitation,[9] or syntheses in related hydrofluxes.[14] This highlights a specificity of the hydrofluxes probed herein, beyond phase selection. This growth behavior along the ***c*** direction is

https://doi.org/10.26434/chemrxiv-2024-lk8q5 **ORCID:** https://orcid.org/0000-0003-4914-4913 Content not peer-reviewed by ChemRxiv. **License:** CC BY 4.0

similar to the growth of calcium phosphate hydroxyapatite rods in water driven by surface energy minimization,[20] in agreement with the identical crystal structure.

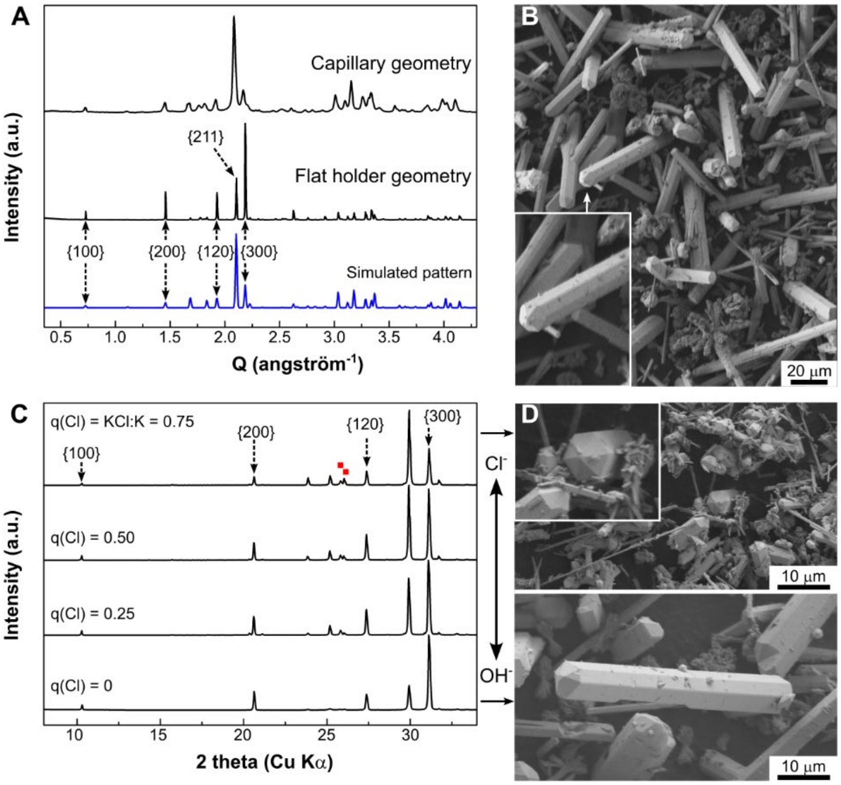

Figure 3. Anisotropic growth of $Sr_5(MnO_4)_3OH$ in hydrofluxes. (A) Powder XRD patterns for the sample obtained at ($q(H_2O)_K$, q(Sr)) = (2.8, 4.0), recorded in flat geometry favoring preferential orientation (as in **Figure 2** and **Figures S1-S3**), in capillary geometry and transmission mode under synchrotron radiation to limit preferential orientation, and simulated according to the tabulated structure. (B) Corresponding SEM image. Role of the hydroxide content in the hydroflux, probed by varying the KCl content with q(Cl) = KCl:K ratio for ($q(H_2O)_K$, q(Sr)) = (2.8, 4.0): (C) XRD patterns and (D) corresponding SEM images of the products. All diffraction peaks belong to the hydroxyapatite structure, except those labeled with red squares, corresponding to $SrCO_3$ impurities.

Anisotropic growth shows a strong dependence on the hydroflux composition. Indeed, for q(Sr) = 2.0 and 4.0, in the hydrofluxes containing the largest amounts of water, an increase of $q(H_2O)_K$ from 2.2 to 2.8 (**Figure S4**), hence an increase in the water content, yields an increase of anisotropy. Previously reported syntheses of $Sr_5(MnO_4)_3OH$ by precipitation in strongly alkaline

https://doi.org/10.26434/chemrxiv-2024-lk8q5 **ORCID:** https://orcid.org/0000-0003-4914-4913 Content not peer-reviewed by ChemRxiv. **License:** CC BY 4.0

aqueous solutions indicate the onset of crystallization around 100 °C.[9] For $q(H_2O)_A$ equal to 2.8, 2.2, the molar fractions of *A*OH are 26 and 31 %, respectively, which correspond to melting points below 100 °C,[21] thus the KOH-based hydrofluxes yielding the hydroxyapatite are liquid at the crystallization onset. Two effects can be accounted for the evolution of anisotropy with the water content: a change in the solubility of the precursors, especially strontium as it is poorly soluble in strongly alkaline media, or a change in the energies of interfaces between the growing crystal and the hydroflux. Several analyses and experiments were then performed to decipher these two effects.

First, to evaluate the concentration of Sr^{2+} available in the liquid phase close to the nucleation temperature, we made the rough assumption that at 100 °C, the reaction medium behaves as a saturated $Sr(OH)_2$ solution (see **supplementary text 1**). Although this approximation does not capture the specificity of the solvating behavior of hydrofluxes, it is instructive in providing a hint at the possible evolution of the strontium concentration in the liquid media. The Sr^{2+} concentration is doubled when $q(H_2O)_K$ increases from 2.2 to 2.8 so this parameter could play a role in anisotropic growth.

To further decipher the importance of the OH^- and Sr^{2+} concentrations on anisotropic growth, we substituted KOH with KCl in the hydroflux. The H_2O:K ratio ($q(H_2O)_K$ value) is then maintained while OH^- ions are replaced by Cl^-, decreasing the basicity of the hydroflux. We then introduce a new parameter, $q(Cl)$, to quantify the extent of substitution: $q(Cl)$ = KCl:K molar ratio. The reactions were performed for ($q(H_2O)_K$, $q(Sr)$) = (2.8, 4.0) and varying $q(Cl)$. The corresponding XRD patterns are displayed in **Figure 3C**. When $q(Cl)$ increases, the preferential orientation is strongly reduced and totally vanishes at $q(Cl) = 0.75$, with relative intensities in agreement with the simulated pattern (**Figure 3C**). The loss of control over anisotropic growth for low hydroxide contents is confirmed by SEM images (**Figures 3D**) with a large polydispersity arising at high $q(Cl)$. These data confirm that the OH^- content of the hydroflux is a key factor influencing the anisotropic growth of $Sr_5(MnO_4)_3OH$ crystals. The Sr^{2+} concentrations calculated near the crystallization onset with the same assumptions as mentioned above (see **supplementary text 1**) show that the concentration of solubilized Sr^{2+} increases as $q(Cl)$ increases, as for an increase of $q(H_2O)_K$, but anisotropy do not increase accordingly: it is favored for $q(Cl)$ decreasing and $q(H_2O)_K$ increasing. Therefore, we rule out a possible impact of the Sr^{2+} concentration at the crystallization onset on anisotropic growth.

https://doi.org/10.26434/chemrxiv-2024-lk8q5 ORCID: https://orcid.org/0000-0003-4914-4913 Content not peer-reviewed by ChemRxiv. License: CC BY 4.0

To confirm this interpretation, we assessed the impact of the Sr precursor on anisotropic growth, by reacting several Sr sources (strontium hydroxide, strontium chloride, and strontium nitrate) at constant ($q(H_2O)_K$), q(Sr), q(Cl)) values of (2.8, 4.0, 0), as in **Figure 2**. XRD (**Figure S8**) shows that while $Sr(OH)_2$ yields the strongest crystal anisotropy, the preferential $\{hk0\}$ orientation is reduced with strontium chloride and disappears when using strontium nitrate, indicating that anisotropic growth is hindered. In these conditions, strontium chloride or nitrate readily convert to strontium hydroxide (see **supplementary text 2**), so that the nature of Sr species and the Sr^{2+} concentration close to the onset of crystallization are similar to the one when starting directly from strontium hydroxide as the precursor. This confirms that the Sr^{2+} concentration cannot account for the difference in anisotropic growth.

Therefore, we propose that the anisotropic growth of hydroxyapatite crystals and its dependence upon the hydrofluxes composition (water content, hydroxide content) is directly linked to the interaction between the hydroflux and the crystal facets. Indeed, Susman, Rimer, *et al.*[22] observed that adding small amounts of water to a $NaNO_3$:KNO_3 (3:2 at.) molten mixture favored the growth of MgO crystals exposing rare {111} facets. Faceting was explained by the preferential interaction of water molecules with the {111} MgO facets. For the archetypal calcium phosphate hydroxyapatites, water interacts preferentially with the {100} facets, leading to preferential growth along the ***c*** axis.[20,23,24] We observe herein a similar trend for a Mn(V) hydroxyapatite: the preferential [001] growth can be ascribed to stabilization of the {100} facets by interaction with water molecules that decrease their surface energy. Interestingly, foreign anions, including nitrate and chloride ions, seem to disturb the interaction of water molecules with {100} facets, possibly by competitive adsorption. These species could also change the local structure of the hydroflux, by preferential interaction with water, alkali cations, or hydroxide anions; We note that previous reports of Mn(V) hydroxyapatite syntheses used strontium chloride for precipitation in strongly alkaline aqueous solutions[9] or strontium nitrate by hydroflux synthesis.[14] In agreement with our interpretation, these works could not achieve anisotropic growth.

Synthesis of hydroxyapatite at the nanoscale

Although **Figure 2B** displays general trends for speciation in NaOH-based hydrofluxes, the nature of minor products suggests additional richness for the design of hydroxyapatite phases. Indeed,

https://doi.org/10.26434/chemrxiv-2024-lk8q5 **ORCID:** https://orcid.org/0000-0003-4914-4913 Content not peer-reviewed by ChemRxiv. **License:** CC BY 4.0

the $Sr_5(MnO_4)_3OH$ structure can be detected as secondary phase for q(Na) = 1 and q(Sr)) ≤ 2 (**Figure S7A**), hence away from the predominance area for $Sr_5(MnO_4)_3OH$ as main product. In these conditions and contrary to all other compositions probed without Cl^- ions by using $Sr(OH)_2$, the relative intensities of the hydroxyapatite XRD peaks are consistent with those expected from the tabulated crystal structure, indicating no marked anisotropic growth. The corresponding reflections are also broader than in other conditions, suggesting a smaller size of crystalline domains. We then explored smaller $q(H_2O)_{Na}$ values, hence lower water content, to isolate this specific form of hydroxyapatite. At $q(H_2O)_{Na}$ = 0.5, according to XRD (**Figure 4A**), no matter the q(Sr) value, $Sr_5(MnO_4)_3OH$ is the only crystalline Mn phase. The only byproduct is $SrCO_3$, more prominent at high q(Sr) due to the excess of $Sr(OH)_2$ supplied to the reaction medium and its strong tendency to carbonation. No significant preferential orientation is detected. The corresponding peaks are again wider than in the large $q(H_2O)_A$ range (**Figure 2C**), suggesting smaller crystallites. They also exhibit a significant shift to large angles compared to the simulated pattern. We focus on the ($q(H_2O)_{Na}$, q(Sr)) = (0.5, 1.0) conditions that provide the hydroxyapatite with the highest purity according to XRD.

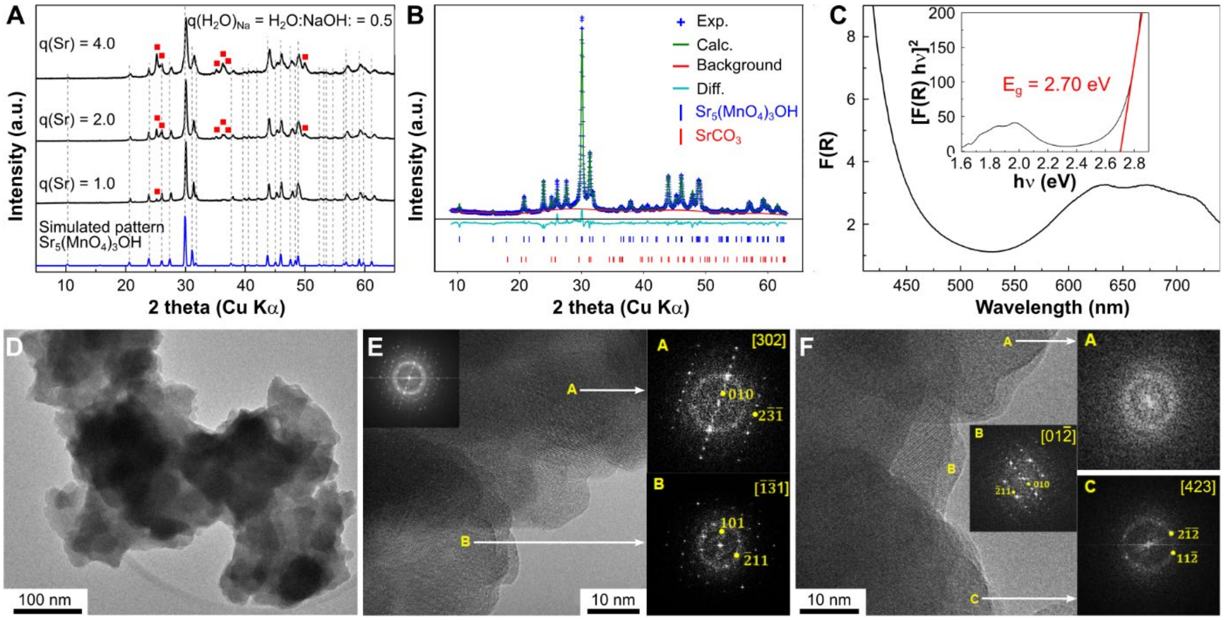

Figure 4. Nanostructured Mn(V) hydroxyapatite. (A) XRD patterns of powders obtained by varying the Sr:Mn ratio in NaOH-based hydrofluxes with low water content: $q(H_2O)_{Na} = H_2O$:NaOH = 0.5. Red squares correspond to $SrCO_3$ impurity. (B) Powder XRD pattern and corresponding Rietveld refinement for the sample obtained at ($q(H_2O)_{Na}$, q(Sr)) = (0.5, 1.0), recorded in a flat geometry. (C) UV-visible spectrum and its Tauc plot analysis. Corresponding (D) TEM and (D-F) HRTEM images with FFTs showing crystalline domains that

https://doi.org/10.26434/chemrxiv-2024-lk8q5 **ORCID:** https://orcid.org/0000-0003-4914-4913 Content not peer-reviewed by ChemRxiv. **License:** CC BY 4.0

can be indexed along the hydroxyapatite structure. The FFT in zone A of (F) highlights an amorphous area.

Wavelength-dispersive X-ray fluorescence (WDXRF) indicates Sr:Mn and Na:Mn ratios equal to 1.6 and 0.1, respectively, compared to 1.6 and 0 measured for hydroxyapatites obtained in other condition areas (**Figure 2**). This suggests a strong default of Sr^{2+} cations, in agreement with the Sr:Mn reagents ratio, and a significant amount of sodium for the apatite obtained at low $q(H_2O)_{Na}$. Rietveld refinement (**Figure 4B** and **Table S2**) indicates an *a* lattice parameter of 9.887 Å, considerably below the tabulated value (9.953 Å), while the *c* parameter does not show any significant deviation, so that the cell is smaller than the ideal structure. Fourier-transform infrared spectroscopy (FTIR) (**Figure S9**), shows two bands at 752 and 798 cm^{-1}, which correspond to υ_3 (E_u) and υ_3 (A_{1u}), vibration modes of MnO_4^{3-} tetrahedra, respectively.[14] The UV-visible spectrum (**Figure 4C**) shows a minimum of diffuse reflectance at 530 nm, consistent with the material's green color, characteristic of hydroxyapatites containing large amounts of Mn(V) tetrahedra.[13] The Tauc plot analysis indicates a direct band gap of 2.7 eV, which was not reported before. Therefore, the material is still based on a Mn(V)-based hydroxyapatite structure. This structure provides a versatile framework for isovalent and aliovalent ion substitutions:[25] while OH^- in the structural channels can be substituted by F^- in $Sr_5(MnO_4)_3OH$,[9] cationic substitution was also reported on Mn site, where Si^{4+} replaces Mn^{5+}.[9] For the most studied calcium phosphate hydroxyapatite $Ca_5(PO_4)_3OH$, substitution of the alkaline earth cation Ca^{2+} has been widely investigated:[25] alkali cations such as Na^+ can substitute Ca^{2+}, which is accompanied by release of OH^- from the channels along the ***c*** axis for charge compensation. This results in a decrease of the *a* lattice parameter.[25,26] An identical trend is observed herein for the Mn(V) hydroxyapatite, hence we suggest Sr^{2+} substitution by Na^+ and the release of OH^- when the synthesis is performed at low $q(H_2O)_{Na}$. The resulting compound is a quinary phase $Na_xSr_{5-x}(MnO_4)_3(OH)_{1-x}$, which agrees with the low Sr:Mn ratio measured by WDXRF. We therefore demonstrate that Mn(V) hydroxyapatites can be a versatile platform for cationic substitution and the synthesis of new materials.

Sodium is in large excess versus manganese and strontium at all compositions probed (Na:Mn = 211 atomic ratio), so that Na^+ doping when moving from high to low $q(H_2O)_{Na}$ can only be linked to the amount of water (pH_2O value) introduced in the reaction medium, hence to the basicity of the hydroflux. The substitution of Sr^{2+} by Na^+ may be related to the very low solubility

https://doi.org/10.26434/chemrxiv-2024-lk8q5 **ORCID:** https://orcid.org/0000-0003-4914-4913 Content not peer-reviewed by ChemRxiv. **License:** CC BY 4.0

of Sr^{2+} at $q(H_2O)_{Na}$ = 0.5 at the crystallization onset (see **supplementary text 1**). In such conditions, the large excess of Na^+ versus Sr^{2+} in solution facilitates incorporation of the alkali cation. Another hypothesis this time related to the crystal growth step is that as $p(H_2O)_{Na}$ increases, speciation in the hydroflux evolves: Sr may form some (hydr)oxoanions as reported for other metals,[14,17] and the water-poor hydroflux may act as good alkali cation donor. Both hypotheses are in line with the formation of alkali-containing phases in hydrofluxes with low amounts of water, as exemplified by $KSrMnO_4$ above and the speciation between $BaNa[Rh(OH)_6]$ and $Ba_3[Rh(OH)_6]_2 \cdot H_2O$ in the Ba-Rh-O system.[27,28]

High Resolution transmission electron images (HRTEM) of the $Na_xSr_{5-x}(MnO_4)_3(OH)_{1-x}$ (**Figures 4D-F**) show that the material is nanostructured and encompasses aggregated particles of 20-30 nm size (**Figure 3F**, zone A) in agreement with XRD data. These particles are embedded into non-crystalline areas. From the corresponding fast Fourier transforms (FFT), all maxima can be indexed on the basis of the hexagonal lattice according to the cell parameters determined from XRD. Local particle by particle STEM-EDS analysis yields Sr:Mn and Na:Mn ratios of 1.7 and 0.04, consistent with WDXRF given measurement uncertainties, in both crystalline and amorphous areas. Such amorphous regions could not be detected by electron microscopy in the hydroxyapatite samples at higher $q(H_2O)_A$ probably indicating a change in the crystallization mechanism. Indeed, in a strongly basic hydroflux, the very low solubility of Sr^{2+} during the onset of crystallization (see **supplementary text 1**) would hinder nucleation from the liquid phase, causing a switch from a liquid-mediated mechanism to solid-state crystallization from an amorphous precursor phase precipitated at the beginning of the process, as is the case for calcium phosphate hydroxyapatite.[23] Upon crystallization from the amorphous precursor, the morphology of the latter is retained and no anisotropic growth occurs. Therefore, we demonstrate control of the micro-/nanostructure of Mn(V) hydroxyapatites. Note however that the speciation of dissolved strontium in highly basic hydrofluxes may also change, as shown for other metals, and then impact the crystallization pathway by first triggering precipitation of an amorphous phase.[14,17]

Raman spectroscopy provides additional evidence of Mn(V) in the form of bands typical of $[MnO_4]^{3-}$ tetrahedra (**Figure 5**, **Table S3**).[13] Additional bands at 400-700 cm^{-1} region are related to a hexagonal $SrMnO_3$ (h-$SrMnO_3$),[29] which highlights the presence of Mn(IV) species. These bands are significantly more intense in the nanostructured materials at ($q(H_2O)_{Na}$, $q(Sr)$) = (0.5, 1.0) than in the well-crystallized hydroxyapatite made of microrods at ($q(H_2O)_K$, $q(Sr)$) =

https://doi.org/10.26434/chemrxiv-2024-lk8q5 ORCID: https://orcid.org/0000-0003-4914-4913 Content not peer-reviewed by ChemRxiv. License: CC BY 4.0

(2.8, 1.0), which suggests that Mn(IV) is found mostly in the amorphous component detected by TEM (**Figure 3F**). This speciation between the nanocrystalline and amorphous domains can be ascribed to the poor stability of the amorphous phase and possibly to the rapid precipitation of this amorphous material.

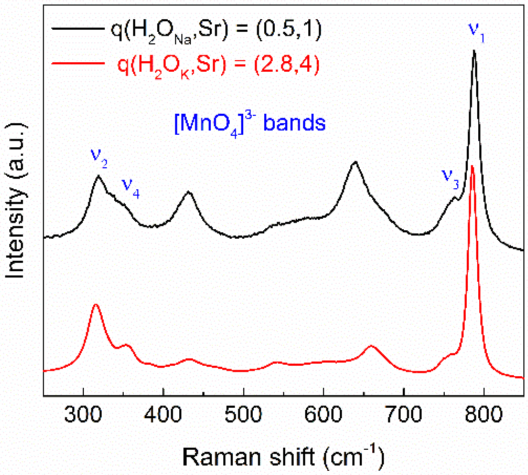

Figure 5. Raman spectra of hydroxyapatite samples: microrods obtained at ($q(H_2O)_{Na}$, $q(Sr)$) = (0.5, 1.0) and nanostructured material synthesized at ($q(H_2O)_K$, $q(Sr)$) = (2.8, 4.0).

Evaluation of pentavalent manganese oxide towards electrocatalytic water oxidation

To evaluate the opportunities of using the Mn(V) hydroxyapatite for oxidizing water,[30] we focused on the nanostructured hydroxyapatite to maximize the surface area exposed to the electrolyte. The open-circuit potential (OCP) is 1.42 V *vs* RHE in 1 M KOH; which is already above the thermodynamic potential for OER (1.23 V *vs* RHE), thus suggesting that Mn(V) is not stable in such conditions. Indeed, cyclic voltammograms recorded in the same electrolyte at 20 mV s^{-1} (**Figure 6A**) show an OER onset potential around 1.60 V *vs* RHE, an activation of the material over the first 5 cycles, and the concomitant growth of a reversible reduction wave, which keeps increasing upon cycling. The redox wave with oxidation and reduction peaks at 1.49 and 1.28 V *vs* RHE, respectively, indicates a Mn(VII)/Mn(VI) couple.[31] Accordingly, the electrolyte became purple. This indicates the release of permanganate. Mayhofer *et al.* reported a similar behavior for manganese-based oxides[32] that degrade and produce permanganate at OER potentials. This is also

https://doi.org/10.26434/chemrxiv-2024-lk8q5 **ORCID:** https://orcid.org/0000-0003-4914-4913 Content not peer-reviewed by ChemRxiv. **License:** CC BY 4.0

in agreement with the work of Rabe *et al.*[33] who reported the dissolution of Mn as permanganate when a manganese oxide electrocatalyst was submitted to an OER potential in a 0.1 M NaOH electrolyte. In addition, a simultaneous deposition of MnO_2 during manganese dissolution during OER has been previously proposed.[33] This mechanism is likely related to the activation of OER (**Figure 6A**).

The electrode was exhaustively rinsed with 1 M KOH solution before being introduced in the electrochemical cell again with fresh electrolyte. A new sequence of 15 voltammograms was recorded, by ensuring that the potential window is above the OCP (**Figure 6B**). The OER onset potential remained unchanged, although the Mn(VII)/Mn(VI) redox waves disappeared. We did not observe any evolution of the OER current upon cycling. The electrolyte near the electrode became again purple, but at a lower extent than in the previous experiment. The electrode was then soaked into the electrolyte overnight at OCP. It recovered an intense green color. 50 new cyclic voltammograms were recorded (**Figure 6C**) and showed similar activity as above. The appearance of the green color in the electrolyte may be associated with the formation of MnO_4^{2-} by MnO_4^- reduction in an alkaline environment,[14] which is a slow reaction.[34]

Different manganese oxides, have been studied towards OER electrocatalysis in 1 M KOH by Heese-Gärtein *et al.*[35] The activity presented herein after activation, hence after evolution of the hydroxyapatite, is similar to the most active material reported by the authors, cryptomelane, and suggests that the hydroxyapatite surface evolves into a MnO_2-based phase by solid-stat transformation or by dissolution-redeposition.[32]

https://doi.org/10.26434/chemrxiv-2024-lk8q5 **ORCID:** https://orcid.org/0000-0003-4914-4913 Content not peer-reviewed by ChemRxiv. **License:** CC BY 4.0

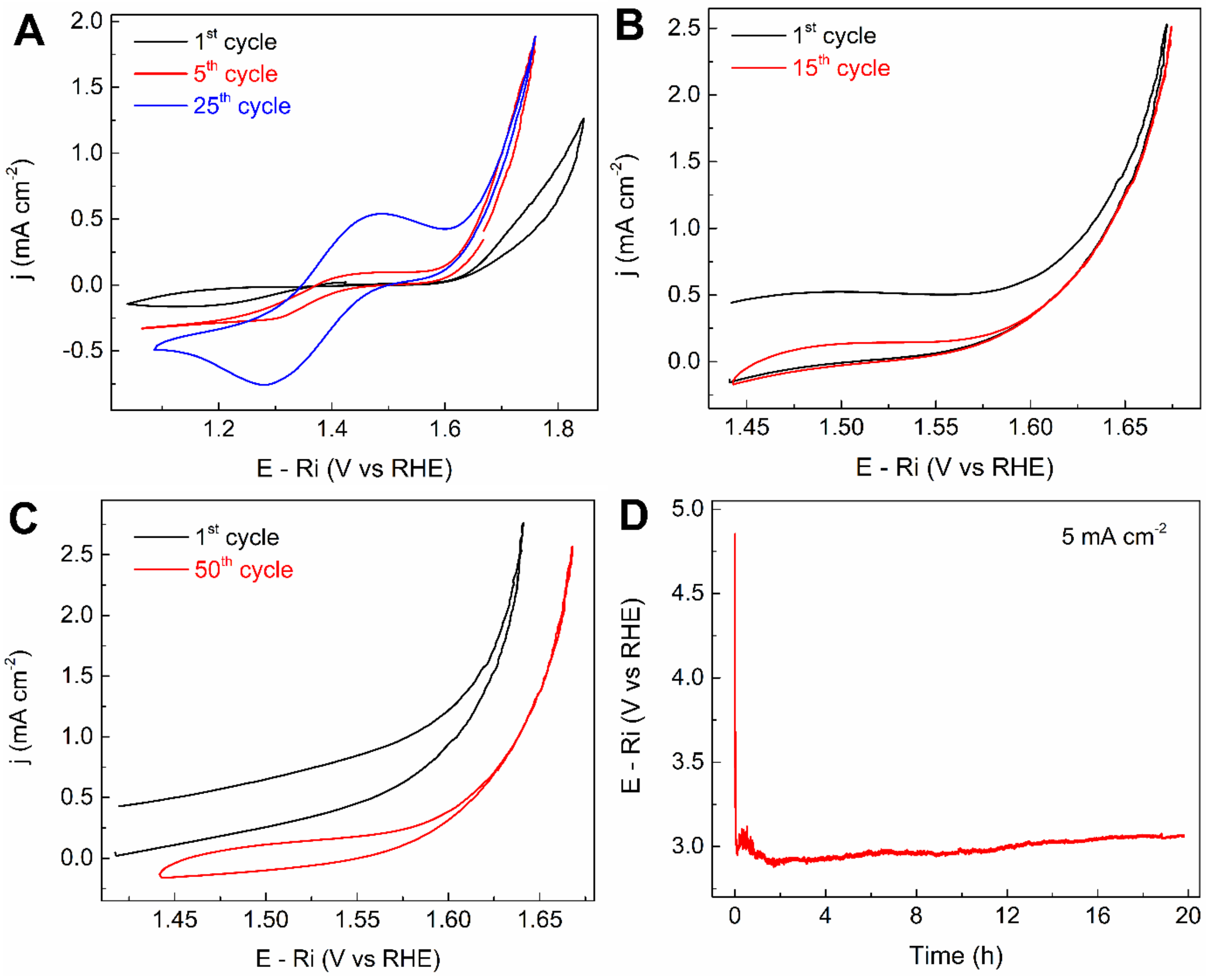

Figure 6. Electrochemical behavior of nanostructured hydroxyapatite. CV analyses with (A) extended potential window, (B) lowest potential limited to the open circuit voltage (OCP), and (C) after soaking the electrode at OCP. **(D)** Chronopotentiometry measurement at 5 mA cm^{-2} with a fresh $Na_xSr_{5-x}(MnO_4)_3OH$ electrode in a 1 M KOH electrolyte.

To avoid decomposition into permanganate, we assessed the possibility of maintaining the electrode at a sufficiently high potential by performing chronopotentiometry (CP) at 5 mA cm^{-2} for 20 h (**Figure 4D**). Some OER activation of material is verified in the first 1.5 h, achieving a value of 2.90 V vs RHE at this time. Then, the electrochemical response retained a good electrochemical stability, only showing a 5.5 % potential increase after 20 h. Noteworthy, no coloring of the electrolyte occurred, neither at the electrode surface nor at the electrolyte, which corroborates material stability. Meanwhile, we observe the evolution of O_2 bubbles from the electrode. Nonetheless, reaching such a current density requires a high potential, thus further

https://doi.org/10.26434/chemrxiv-2024-lk8q5 ORCID: https://orcid.org/0000-0003-4914-4913 Content not peer-reviewed by ChemRxiv. License: CC BY 4.0

supporting the interpretation that the OER activity measured upon cyclic voltammetry (**Figure 4B-C**) arises from a MnO_2-type electrocatalytic material forming at the surface of the material.

Nonetheless, this study demonstrates the feasibility of preventing the degradation of Mn(V) compounds. This stability at elevated potentials as 3 V *vs* RHE, with low rates of O_2 evolution, is an interesting property for electrochemical applications where the reactions of interest compete with OER, like in wastewater treatment.[36]

Conclusion

We have built a rational framework of phase speciation and particle shape tuning by applying a multi-parametric study of the syntheses of Mn(V) oxides in hydrofluxes. The guidelines to achieve such control encompass the selection of the alkali hydroxide component of the hydroflux, the control of the oxidative power and the alkali donor habit of the hydroflux, and the water content. The latter provides not only control over facet stabilization and then shape for the first time, it also enables phase selection. The water content also seems to offer the ability to tune the crystallization pathway of Mn(V) hydroxyapatites, switching between liquid-phase and solid-state crystallization mechanisms, with a large impact on the control of the nanostructure. By defining the acid-base-redox stability window of a Mn(V) hydroxyapatite in alkaline media, we demonstrate that hydrofluxes are a versatile platform, which offers materials standing strongly oxidative conditions.

ASSOCIATED CONTENT

Supporting Information Available: XRD patterns of products obtained in different synthesis conditions (Figures S1-S8), summary of phase speciation according to XRD (Table S1), valuation of Sr^{2+} solubility (supplementary texts 1 and 2), details of Retveld refinement for nanostructured hydroxyapatite (Table S2), corresponding FTIR spectrum (Figure S9) and Raman band postions (Table S3).

ACKNOWLEDGMENTS

This work was funded by the *Agence Nationale de la Recherche* (ANR, Grant No. ANR-21-CE50-0021). M.P, A.V and A. T. P acknowledge the support from "(MAD2D-CM)-UCM" and PR65/19-

https://doi.org/10.26434/chemrxiv-2024-lk8q5 **ORCID:** https://orcid.org/0000-0003-4914-4913 Content not peer-reviewed by ChemRxiv. **License:** CC BY 4.0

22438 Research Projects funded by Comunidad de Madrid and from the Ministerio de Ciencia, Innovación y Universidades through Research Project PID2020-113753RB-I00. The Federation of Chemistry and Materials of Paris-Center (FCMat) is gratefully acknowledged for SEM experiments. SEM was funded by Sorbonne Université, CNRS and Région Ile de France. We acknowledge the European Synchrotron Radiation Facility (ESRF) for provision of synchrotron radiation facilities under proposal number MA-5619.

EXPERIMENTAL METHODS

Reagents

KOH (85%, Alfa Aesar), KCl (99%, Sigma-Aldrich) NaOH (98%, Sigma-Aldrich), $Sr(OH)_2 \cdot 8 H_2O$ (95%, Sigma-Aldrich), $Sr(NO_3)_2$ (99%, Sigma-Aldrich), $SrCl_2 \cdot 6 H_2O$ (99%, Sigma-Aldrich), $KMnO_4$ (99%, Sigma-Aldrich) and $NaMnO_4 \cdot H_2O$ (97%, Sigma-Aldrich) were used as purchased.

Materials synthesis

First, for the synthesis of $Sr_5(MnO_4)_3OH$ at $q(H_2O_K,Sr) = (2.8,4)$, 210 mmol of KOH, 10.2 mL of ultrapure water, 4 mmol of $Sr(OH)_2$ and 1 mmol of $KMnO_4$ were added to a 23 mL Teflon container. It was inserted into an autoclave, which were then placed in an oven and heated at 230 ºC for 12 h with a 5 ºC min^{-1} ramp. It was then cooled down to room temperature. Powders were finally collected after water washing and centrifugation cycles, followed by heating under vacuum overnight at 40 ºC. During all synthesis batches, the Mn:A(K,Na) molar ratio was maintained equal 1:210. Therefore, the adjust of $q(H_2O_A)$ and q(Sr) parameters was done by varying the water and strontium amounts added, respectively. For introducing the q(Cl), KOH was replaced by KCl in hydrofluxes compositions. It is important to notice that manganese sources in potassium hydroxide (KOH) and sodium hydroxide (NaOH) hydroflux were potassium permanganate ($KMnO_4$) and sodium permanganate monohydrate ($NaMnO_4 \cdot H_2O$), respectively. In addition, the hydration water present in the reagents was always considered as part of the total amount of water added.

Characterization

https://doi.org/10.26434/chemrxiv-2024-lk8q5 ORCID: https://orcid.org/0000-0003-4914-4913 Content not peer-reviewed by ChemRxiv. License: CC BY 4.0

X-ray diffraction (XRD) patterns originated from flat holder geometry, which was the standard in this article unless otherwise stated. They were acquired on a Bruker D8 Discover diffractometer, operated under a θ-θ Bragg-Brentano configuration. The X-ray source was a sealed copper anode with $K_{\alpha 1}$ and $K_{\alpha 2}$ emission lines, applying an acceleration tension of 40 kV and 30 mA current. Diffracted X-ray was detected with a LynxEye linear detector. Reference patterns used for $SrCO_3$, $SrMnO_3$, $KSrMnO_4$, $Sr_5(MnO_4)_3OH$ and $Na_{0.7}MnO_2$ were PDF cards 01-074-1491, 01-072-0197, 01-089-9532, 01-090-3690 and 01-090-2314, respectively. Rietveld refinement was performed using the GSAS-II software.[37]

Synchrotron-based X-ray diffraction was carried out at the ESRF synchrotron on beamline ID11, in transmission mode at an energy (wavelength) of 93.3159 keV (0.1329 Å). A Double Crystal Monochromator equipped with two Si(111) crystals was used to tune the energy. The detector was a Frelon4M 2048 × 2048 16Bit fast CCD Camera.

Scanning electron microscopy (SEM) was performed in a FEG-SEM Hitachi SU-70, with acceleration voltage set at 2 kV for image acquisition in secondary electron mode without coating the samples.

UV-Vis spectroscopy was performed in an Agilent Technologies Cary Series 5000 UV-visible-near-infrared spectrometer, which used a double beam with FTO background reference.

Transmission electron microscopy (TEM). Electron microscopy was performed using the equipment situated in the National Facility ELECMI ICTS facilities. Selected area electron diffraction (SAED), high-resolution electron microscopy (HREM) and crystal by crystal chemical microanalysis were performed using a JEOL JEMARM200cF aberration corrected STEM electron microscope (Cold Emission Gun) operating at 80 kV (probe size ~0.08 nm) provided with an EDS Oxford INCA-350 detector.

Vibrational Raman spectroscopy Spectra were taken directly from dry powders. Raman spectra were recorded using an Horiba Xplora spectrometer, equipped with a confocal microscope. The sample was observed using a 10× objective lens before using an Olympus LM Plan FLN 100×

https://doi.org/10.26434/chemrxiv-2024-lk8q5 ORCID: https://orcid.org/0000-0003-4914-4913 Content not peer-reviewed by ChemRxiv. License: CC BY 4.0

objective lens (*N.A.* = 0.80, *W.D.* = 3.4 mm) to focus the laser on the sample and collect the scattered light. A long-pass edge filter was used to remove the fundamental line from the collected scattered light. A 100 mW TE-Cooled, DPSS Laser (λ = 532 nm) was used as the excitation source. Neutral density filters, aperture size, and integration time were chosen to maximize the signal-to-noise ratio. A 600 mm^{-1} grating alongside a Syncerity TE-cooled FI–UV–vis detector to analyze the collected light.

Fourier-transform infrared spectroscopy was performed in a Spectrum® 400 FT-IR/FT-NIR Spectrometer (PerkinElmer) with a universal ATR sampling accessory. The spectrum was obtained after four scans of the dry powder.

Wavelength-dispersive X-ray fluorescence (WDXRF) was performed using an S8 Tiger spectrometer supplied by Bruker, which uses a rhodium anode tube as an X-ray source. The materials were prepared for analysis by pressing them on the top of a previously prepared cellulose pellet.

Preparation of working electrodes. 75 mg of the powder was pressed to produce an 8 mm diameter pellet, which was further attached, with a double-face carbon tape, to the glass carbon substrate of a rotating disk electrode (RDE) tip. A commercial rotating system was provided by BioLogic.

Electrochemical measurements were performed at room temperature in a three-electrode cell configuration using a potentiostat device (AMETEK Solartron Analytical Modulab). Graphite rod and KCl-saturated Ag/AgCl electrode were employed as counter- and reference electrodes, respectively. Measured potentials were converted according to the following equation:

$$E_{\mathrm{RHE}} = E_{\mathrm{measured}} + 0.197 + 0.0591 \times \mathrm{pH} \qquad \textbf{(7)}$$

Experiments were carried out in a 1 M KOH (Pellets for analysis EMSURE) electrolyte while applying a rotation speed of 1600 rpm for the working electrode. Electrochemical impedance spectroscopy (EIS) was performed at open-circuit potential (OCP) to obtain the solution resistance

https://doi.org/10.26434/chemrxiv-2024-lk8q5 **ORCID:** https://orcid.org/0000-0003-4914-4913 Content not peer-reviewed by ChemRxiv. **License:** CC BY 4.0

(R_s) values, which were further used for the ohmic drop compensation. Cyclic voltammetry (CV) analyses were performed at 20 mV s^{-1} and chronopotentiometry (CP) analysis was performed at 5 mA cm^{-2} during 20 h.

https://doi.org/10.26434/chemrxiv-2024-lk8q5 **ORCID:** https://orcid.org/0000-0003-4914-4913 Content not peer-reviewed by ChemRxiv. **License:** CC BY 4.0

References

(1) Bernardini, S.; Bellatreccia, F.; Della Ventura, G.; Sodo, A. A Reliable Method for Determining the Oxidation State of Manganese at the Microscale in Mn Oxides *via* Raman Spectroscopy. *Geostand. Geoanalytical Res.* **2021**, *45* (1), 223–244. https://doi.org/10.1111/ggr.12361.

(2) Medina, E. A.; Li, J.; Stalick, J. K.; Subramanian, M. A. Intense Turquoise Colors of Apatite-Type Compounds with Mn^{5+} in Tetrahedral Coordination. *Solid State Sci.* **2016**, *52*, 97–105. https://doi.org/10.1016/j.solidstatesciences.2015.12.001.

(3) Laha, S.; Tamilarasan, S.; Natarajan, S.; Gopalakrishnan, J. Stabilization of a Tetrahedral ($Mn^{5+}O_4$) Chromophore in Ternary Barium Oxides as a Strategy toward Development of New Turquoise/Green-Colored Pigments. *Inorg. Chem.* **2016**, *55* (7), 3508–3514. https://doi.org/10.1021/acs.inorgchem.5b02957.

(4) Moncorgé, R.; Manaa, H.; Boulon, G. Cr^{4+} and Mn^{5+} Active Centers for New Solid State Laser Materials. *Opt. Mater.* **1994**, *4* (1), 139–151. https://doi.org/10.1016/0925-3467(94)90071-X.

(5) Uchida, M.; Tanaka, H.; Bartashevich, M. I.; Goto, T. Singlet Ground State and Magnetization Plateaus in $Ba_3 Mn_2O_8$. *J. Phys. Soc. Jpn.* **2001**, *70* (6), 1790–1793. https://doi.org/10.1143/JPSJ.70.1790.

(6) Koo, H.-J.; Lee, K.-S.; Whangbo, M.-H. Spin Dimer Analysis of the Magnetic Structures of $Ba_3 Cr_2O_8$, $Ba_3Mn_2O_8$, $Na_4 FeO_4$, and Ba_2CoO_4 with a Three-Dimensional Network of Isolated MO_4 (M = Cr, Mn, Fe, Co) Tetrahedra. *Inorg. Chem.* **2006**, *45* (26), 10743–10749. https://doi.org/10.1021/ic061773c.

(7) Ma, L.; Wang, Q.; Man, W.-L.; Kwong, H.-K.; Ko, C.-C.; Lau, T.-C. Cerium(IV)-Driven Water Oxidation Catalyzed by a Manganese(V)-Nitrido Complex. *Angew. Chem. Int. Ed. 54*, 5246–5249. https://doi.org/10.1002/anie.201500507.

(8) Yano, J.; Robblee, J.; Pushkar, Y.; Marcus, M. A.; Bendix, J.; Workman, J. M.; Collins, T. J.; Solomon, E. I.; DeBeer George, S.; Yachandra, V. K. Polarized X-Ray Absorption Spectroscopy of Single-Crystal Mn(V) Complexes Relevant to the Oxygen-Evolving Complex of Photosystem II. *J. Am. Chem. Soc.* **2007**, *129* (43), 12989–13000. https://doi.org/10.1021/ja071286b.

(9) Varela, A.; Gómez-Recio, I.; Serrador, L.; Hernando, M.; Matesanz, E.; Torres-Pardo, A.; Fernández-Díaz, M. T.; Martínez, J. L.; Gonell, F.; Rousse, G.; Sanchez, C.; Laberty-Robert, C.; Portehault, D.; González-Calbet, J. M.; Parras, M. Hydroxyapatites as Versatile Inorganic Hosts of Unusual Pentavalent Manganese Cations. *Chem. Mater.* **2020**, *32* (24), 10584–10593. https://doi.org/10.1021/acs.chemmater.0c03673.

(10) Chance, M. W. Hydroflux Synthesis: A New and Effective Technique for Exploratory Crystal Growth. **2024**, University of South Carolina.

(11) Knyazev, A. V.; Bulanov, E. N.; Smirnova, N. N.; Korshak, K. S.; Xu, Z.; Sarmini, Yu. A. Synthesis, Structure and Thermodynamic Properties of $Ba_5(MnO_4)_3Cl$ Apatite. *J. Chem. Thermodyn.* **2019**, *129*, 30–35. https://doi.org/10.1016/j.jct.2018.09.004.

(12) Grisafe, D. A.; Hummel, F. A. Pentavalent Ion Substitutions in the Apatite Structure Part A. Crystal Chemistry. *J. Solid State Chem.* **1970**, *2* (2), 160–166. https://doi.org/10.1016/0022-4596(70)90064-2.

https://doi.org/10.26434/chemrxiv-2024-lk8q5 **ORCID:** https://orcid.org/0000-0003-4914-4913 Content not peer-reviewed by ChemRxiv. **License:** CC BY 4.0

(13) Dardenne, K.; Vivien, D.; Huguenin, D. Color of Mn(V)-Substituted Apatites $A_{10}((B, Mn)O_4)_6F_2$, A=Ba, Sr, Ca; B=P, V. *J. Solid State Chem.* **1999**, *146* (2), 464–472. https://doi.org/10.1006/jssc.1999.8394.

(14) Albrecht, R.; Doert, T.; Ruck, M. Hydroflux Synthesis and Characterization of the Non-Centrosymmetric. *Z. Für Anorg. Allg. Chem.* **2020**, *646*, 1389–1395. https://doi.org/10.1002/zaac.202000065.

(15) Alonso, J. A.; Martínez-Lope, M. J.; De La Calle, C.; Sánchez-Benítez, J.; Retuerto, M.; Aguadero, A.; Fernandez-Díaz, M. T. High-Pressure Synthesis and Characterization of New metastable Oxides. *Funct. Mater. Lett.* **2011**, *04* (04), 333–336. https://doi.org/10.1142/S1793604711002123.

(16) Pourbaix, M. Atlas d'Equilibres Electrochimiques. Gauthier-Villars & Cie, Paris, **1963**.

(17) Mugavero, S. J.; Gemmill, W. R.; Roof, I. P.; Zur Loye, H.-C. Materials Discovery by Crystal Growth: Lanthanide Metal Containing Oxides of the Platinum Group Metals (Ru, Os, Ir, Rh, Pd, Pt) from Molten Alkali Metal Hydroxides. *J. Solid State Chem.* **2009**, *182* (7), 1950–1963. https://doi.org/10.1016/j.jssc.2009.05.006.

(18) Flood, H.; Förland, T. The Acidic and Basic Properties of Oxides. *Acta Chem. Scand. 1*, 592–604. https://doi.org/10.3891/acta.chem.scand.01-0592.

(19) Tremillon, B. Diagrammes d'Equilibre Potentiel-acidité (pO2-) dans les Sels et Hydroxydes Alcalins Fondus. *Pure Appl. Chem. 25*, 395–428. https://doi.org/10.1351/pac197125020395.

(20) Zhao, W.; Xu, Z.; Yang, Y.; Sahai, N. Surface Energetics of the Hydroxyapatite Nanocrystal–Water Interface: A Molecular Dynamics Study. *Langmuir* **2014**, *30* (44), 13283–13292. https://doi.org/10.1021/la503158p.

(21) Roach, L.; Erriguible, A.; Aymonier, C. Development of Molten Salt–Based Processes through Thermodynamic Evaluation Assisted by Machine Learning. *Chem. Eng. Sci.* **2024**, *299*, 120433. https://doi.org/10.1016/j.ces.2024.120433.

(22) Susman, M. D.; Pham, H. N.; Datye, A. K.; Chinta, S.; Rimer, J. D. Factors Governing MgO(111) Faceting in the Thermal Decomposition of Oxide Precursors. *Chem. Mater.* **2018**, *30* (8), 2641–2650. https://doi.org/10.1021/acs.chemmater.7b05302.

(23) Dalmônico, G. M. L.; Ihiawakrim, D.; Ortiz, N.; Barreto Junior, A. G.; Curitiba Marcellos, C. F.; Farina, M.; Ersen, O.; Rossi, A. L. Live Visualization of the Nucleation and Growth of Needle-Like Hydroxyapatite Crystals in Solution by In Situ TEM. *Cryst. Growth Des.* **2022**, *22* (8), 4828–4837. https://doi.org/10.1021/acs.cgd.2c00296.

(24) Diez-Escudero, A.; Espanol, M.; Ginebra, M.-P. High-Aspect-Ratio Nanostructured Hydroxyapatite: Towards New Functionalities for a Classical Material. *Chem. Sci.* **2024**, *15* (1), 55–76. https://doi.org/10.1039/D3SC05344J.

(25) Šupová, M. Substituted Hydroxyapatites for Biomedical Applications: A Review. *Ceram. Int.* **2015**, *41* (8), 9203–9231. https://doi.org/10.1016/j.ceramint.2015.03.316.

(26) Naqshbandi, A.; Rahman, A. Sodium Doped Hydroxyapatite: Synthesis, Characterization and Zeta Potential Studies. *Mater. Lett.* **2022**, *312*, 131698. https://doi.org/10.1016/j.matlet.2022.131698.

(27) Albrecht, R.; Bretschneider, V.; Doert, T.; Ruck, M. $Ba_3[Rh(OH)_6]_2 \cdot H_2O$ – a Precursor to Barium Oxorhodates with One-dimensional Hydrogen Bonding Systems. *Z. Für Anorg. Allg. Chem.* **2021**, *647* (18), 1702–1708. https://doi.org/10.1002/zaac.202100016.

(28) Cook, D. S.; Clarkson, G. J.; Dawson, D. M.; Ashbrook, S. E.; Fisher, J. M.; Thompsett, D.; Pickup, D. M.; Chadwick, A. V.; Walton, R. I. Alkaline-Earth Rhodium Hydroxides:

https://doi.org/10.26434/chemrxiv-2024-lk8q5 **ORCID:** https://orcid.org/0000-0003-4914-4913 Content not peer-reviewed by ChemRxiv. **License:** CC BY 4.0

Synthesis, Structures, and Thermal Decomposition to Complex Oxides. *Inorg. Chem.* **2018**, *57* (17), 11217–11224. https://doi.org/10.1021/acs.inorgchem.8b01797.

(29) Sacchetti, A.; Baldini, M.; Postorino, P.; Martin, C.; Maignan, A. Raman Spectroscopy on Cubic and Hexagonal $SrMnO_3$. *J. Raman Spectrosc.* **2006**, *37* (5), 591–596. https://doi.org/10.1002/jrs.1484.

(30) Brudvig, G. W. Water Oxidation Chemistry of Photosystem II. *Philos. Trans. R. Soc. B Biol. Sci.* **2008**, *363* (1494), 1211–1219. https://doi.org/10.1098/rstb.2007.2217.

(31) Pugolovkin, L. V.; Levin, E. E.; Arkharova, N. A.; Orekhov, A. S.; Presnov, D. E.; Tsirlina, G. A. Cathodic Deposition of Birnessite from Alkaline Permanganate Solutions: Tools to Control the Current Efficiency, Morphology and Adhesion. *J. Electroanal. Chem.* **2020**, *874*, 114521. https://doi.org/10.1016/j.jelechem.2020.114521.

(32) Villalobos, J.; Golnak, R.; Xi, L.; Schuck, G.; Risch, M. Reversible and Irreversible Processes during Cyclic Voltammetry of an Electrodeposited Manganese Oxide as Catalyst for the Oxygen Evolution Reaction. *J. Phys. Energy* **2020**, *2* (3), 034009. https://doi.org/10.1088/2515-7655/ab9fe2.

(33) Rabe, M.; Toparli, C.; Chen, Y.-H.; Kasian, O.; Mayrhofer, K. J. J.; Erbe, A. Alkaline Manganese Electrochemistry Studied by *in Situ* and *Operando* Spectroscopic Methods – Metal Dissolution, Oxide Formation and Oxygen Evolution. *Phys. Chem. Chem. Phys.* **2019**, *21* (20), 10457–10469. https://doi.org/10.1039/C9CP00911F.

(34) Ferguson, R. H.; Lerch, Wm.; Day, J. E. Permanganate Decomposition in Alkaline Media. *J. Am. Chem. Soc.* **1931**, *53* (1), 126–137. https://doi.org/10.1021/ja01352a018.

(35) Heese-Gärtlein, J.; Rabe, A.; Behrens, M. Challenges in the Application of Manganese Oxide Powders as OER Electrocatalysts: Synthesis, Characterization, Activity and Stability of Nine Different MnxOy Compounds. *Z. Für Anorg. Allg. Chem. 647*, 1363–1372. https://doi.org/10.1002/zaac.202000180.

(36) Moreira, F. C.; Boaventura, R. A. R.; Brillas, E.; Vilar, V. J. P. Electrochemical Advanced Oxidation Processes: A Review on Their Application to Synthetic and Real Wastewaters. *Appl. Catal. B Environ.* **2017**, *202*, 217–261. https://doi.org/10.1016/j.apcatb.2016.08.037.

(37) Toby, B. H.; Von Dreele, R. B. GSAS-II: The Genesis of a Modern Open-Source All Purpose Crystallography Software Package. *J. Appl. Crystallogr. 46* (2), 544–549. https://doi.org/10.1107/S0021889813003531.

https://doi.org/10.26434/chemrxiv-2024-lk8q5 **ORCID:** https://orcid.org/0000-0003-4914-4913 Content not peer-reviewed by ChemRxiv. **License:** CC BY 4.0

Table of Content graphic

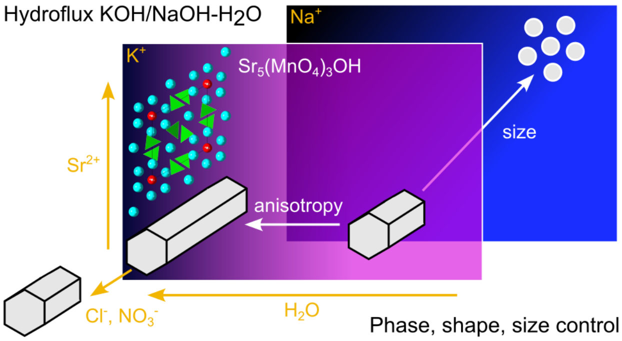

https://doi.org/10.26434/chemrxiv-2024-lk8q5 **ORCID:** https://orcid.org/0000-0003-4914-4913 Content not peer-reviewed by ChemRxiv. **License:** CC BY 4.0